MITORIBOSOME

Mechanism of membrane-tethered mitochondrial protein synthesis

Yuzuru Itoh[1,2]*, Juni Andréll[1,2]*, Austin Choi[3]*, Uwe Richter[4,5,6]*, Priyanka Maiti[3], Robert B. Best[7], Antoni Barrientos[3]†, Brendan J. Battersby[4]†, Alexey Amunts[1,2]†

Mitochondrial ribosomes (mitoribosomes) are tethered to the mitochondrial inner membrane to facilitate the cotranslational membrane insertion of the synthesized proteins. We report cryo–electron microscopy structures of human mitoribosomes with nascent polypeptide, bound to the insertase oxidase assembly 1–like (OXA1L) through three distinct contact sites. OXA1L binding is correlated with a series of conformational changes in the mitoribosomal large subunit that catalyze the delivery of newly synthesized polypeptides. The mechanism relies on the folding of mL45 inside the exit tunnel, forming two specific constriction sites that would limit helix formation of the nascent chain. A gap is formed between the exit and the membrane, making the newly synthesized proteins accessible. Our data elucidate the basis by which mitoribosomes interact with the OXA1L insertase to couple protein synthesis and membrane delivery.

Proteins encoded in the human mitochondrial DNA (mtDNA) are essential for life, and aberrations in their synthesis are associated with clinical pathologies (*1*, *2*). Synthesis of these transmembrane proteins of the oxidative phosphorylation complexes occurs on dedicated mitochondrial ribosomes (mitoribosomes) that have a specialized exit tunnel and regulatory features (*3*). These mitoribosomes are tightly associated with the inner mitochondrial membrane for efficient protein delivery (*4*). Cotranslational membrane insertion is catalyzed by a putative mitochondrial insertase, the oxidase assembly 1–like (OXA1L) protein, a homolog of yeast Oxa1 and bacterial YidC (*5*–*7*). In yeast, Oxa1 is required for the assembly of the oxidative phosphorylation complexes (*8*), and its C terminus is associated with the mitoribosome (*9*, *10*). In human cells, depletion of OXA1L impairs the assembly of the complexes I, IV, and V (*11*, *12*), and biallelic *OXA1L* pathogenic mutations present with fatal encephalitis, hypotonia, and developmental delay (*12*). Mechanistically, the association of the mitoribosome with an insertase would likely protect the hydrophobic membrane proteins during their egression into the lipid bilayer. On the basis of studies of cotranslational folding of membrane proteins into an α-helical conformation in the ribosomal tunnel in bacteria (*13*), it has been postulated that such a secondary structure may also start forming within the mitoribosome tunnel. However, no structure of mitoribosome with a membrane insertase has been reported; thus, a mechanism of nascent-chain emergence remained unknown.

To capture the interactions of a mitoribosomal exit tunnel with its substrate, we used the peptidomimetic actinonin, which structurally resembles formylmethionine, to induce a cotranslational accumulation of stalled mitoribosomes during nascent-chain synthesis (fig. S1) (*14*). To sort the particles corresponding to translating mitoribosomes, we collected six cryo–electron microscopy (cryo-EM) datasets and classified them on the basis of the presence of the small subunit after signal subtraction (*15*). Then, we performed a second step of signal subtraction and three-dimensional (3D) classification on the A-site tRNA and a third step on the insertase region (fig. S2A). Subsequent 3D refinement produced a reconstruction that showed a fragmented density extending from the tunnel exit. To reduce the flexibility of a putative insertase on the mitoribosome, we subjected the complex to amine-to-amine crosslinking and repeated the cryo-EM analysis with two additional datasets (fig. S2, B to F, and

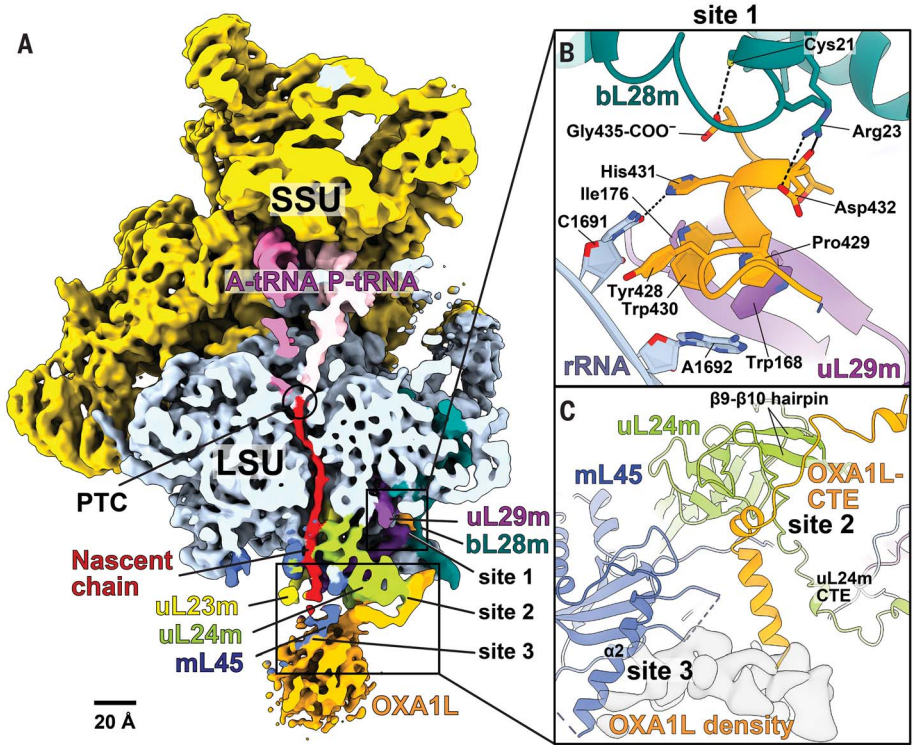

Fig. 1. Human mitoribosome:OXA1L complex. (**A**) Density of mitoribosome:OXA1L complex lowpass filtered to 6-Å resolution for clarity and cut through the tunnel. Contact sites 1, 2, and 3 are indicated. PTC, peptidyl transferase center; LSU, large subunit; SSU, small subunit. (**B**) Contact site 1 is formed by OXA1L C-terminal helix bound to bL28m, uL29m, and rRNA. Tyr^{428} is stacked on rRNA Cys^{1691} (C1691), and His^{431} hydrogen bonds with C1691. The backbone carbonyl and side chain of Asp^{432} form polar interactions with bL28m (Arg^{23}, Pro^{429}, and Trp^{430}) and hydrophobic interactions with uL29m (Trp^{168} and Ile^{176}) and rRNA A1692. (**C**) OXA1L-CTE interacts with uL24m (site 2), and the OXA1L core (shown with density) is associated with mL45-α2 (site 3).

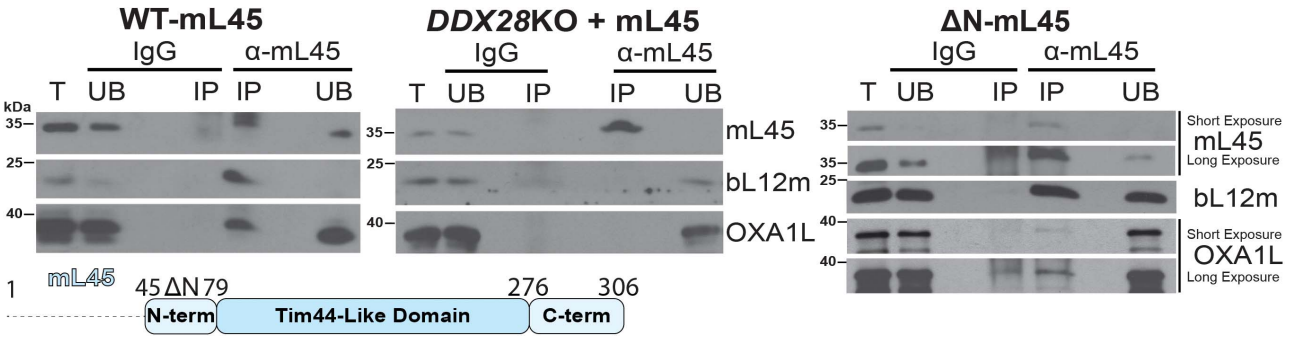

Fig. 2. Biochemical characterization of mL45 and OXA1L interaction. Immunoprecipitation of mL45 from mitochondrial extracts of T-Rex-293 cells expressing WT or Δ*N-mL45* and the *DDX28*-KO (knockout) cells overexpressing WT *mL45*. The cells were probed for mL45, OXA1L, or bL12m as an mtLSU marker, and immunoglobulin G (IgG) was used as a control. IP, immunoprecipitated; T, total input; UB, unbound.

materials and methods). In silico sorting yielded a subset of 30,744 particles that, upon contrast transfer function refinement and Bayesian polishing (*15*), resulted in the 2.89-Å reconstruction, revealing densities for tRNAs in the A- and P-sites, continuous density from the peptidyl transferase center extending to the tunnel exit, and additional mass outside the exit correlating with the position of the inner mitochondrial membrane (*4*) (Fig. 1A and fig. S3). The position of the extra density and its overall dimensions were in agreement with the bacterial ribosome:YidC reconstructions (*16*, *17*) that accommodate a single copy of the insertase (fig. S4).

Although the local resolution for the additional density is 5 to 8 Å, reflecting intrinsic flexibility, by combining biochemical stabilization with targeted classification and polishing, we could improve the signal-to-noise ratio and trace ~50 amino acid residues that were docked to the surface of the mitoribosomal large subunit (mtLSU) (fig. S5). The quality of the side-chain densities was sufficient for modeling the C-terminal residues of OXA1L (fig. S5D), and mass-spectrometry analysis confirmed the presence of OXA1L (fig. S6). OXA1L binds to the mitoribosome through three distinct contact sites spanning the solvent-exposed side of the mtLSU (Fig. 1A and fig. S7). Together, the interface anchoring OXA1L involves three mitoribosomal proteins and ribosomal RNA (rRNA), comprising a total buried surface area of ~1500 Å^2.

Site 1 is found in the mitoribosomal cleft toward the L1 stalk, ~70 Å away from the membrane surface (Fig. 1, A and B). It comprises mitochondrial-specific protein extensions of bL28m, uL29m, and the rRNA bypass element H4-H8 (residues 1689 to 1695) that together form the binding pocket for the OXA1L C-terminal helix (YPWHDTLG-COO$^-$) (fig. S8, A and B). A series of interactions involve residues that are generally conserved in vertebrates and underlie a tight association that does not occur in bacteria (fig. S9).

Site 2 is separated from site 1 by 27 Å and consists solely of the mitoribosomal protein uL24m (Fig. 1C). Although the part of OXA1L linking the two contact sites is not well resolved, we could model 40 residues composed of an α helix, two short 3_{10}-helices, and a 10-residue loop. Together, it binds to the matrix-exposed surface, thus encompassing uL24m, and the loop is stabilized by the β9-β10 hairpin (residues 133 to 147) at the C-terminal domain of uL24m (Fig. 1C and fig. S9D). Consistent with the shape of uL24m, the OXA1L structure is bent in this region by ~80° (Fig. 1, A and C).

Site 3 is ~15 Å away from site 2 and formed by the core domain of mL45, where the globular density of the OXA1L membrane part is attached (Fig. 1C). Although no OXA1L model could be placed here because of the flexibility, continuous density can be traced from the α helix of OXA1L C-terminal extension (CTE) at site 2 (Fig. 1A). The contact is mostly through the α-helix mL45-α2 (residues 94 to 128) on top of the core β sheet of the mL45 Tim44-like domain. Overall, the observed interactions of OXA1L with the mitoribosome are consistent with super-resolution microscopy showing that the CTE truncation (Δ332–433) of OXA1L reduces, but does not completely abolish, the colocalization with the translating mitoribosome (*18*).

Consistent with the structure, we find that OXA1L forms a stable interaction with mL45 in vitro only when it is assembled into the mitoribosome (Fig. 2 and fig. S10). To demonstrate this, we used a cell line in which the mtLSU assembly helicase DDX28 has been deleted (*19*). We ectopically expressed mL45, which associates with the mitochondrial membranes despite the mtLSU assembly defect but does not interact with OXA1L (Fig. 2 and fig. S10). Thus, the interaction between OXA1L and mitoribosomes is mediated by mitoribosome-assembled mL45.

Next, we examined the cryo-EM data with respect to the exit tunnel interior and identified two distinct states, Class 1a* and Class 1b* (figs. S2B and S11). The particles in Class 1b* represent the OXA1L-unbound (inactive) state. The density in the upper tunnel is separated from the tRNA by 12 Å (fig. S11A). This density extends from mL45 and corresponds to its N-terminal sequence, consistent with a previous study (*20*). The previous study also proposed that the mL45 N-terminal tail acts to recruit the OXA1L insertase, implying a targeting mechanism in mammalian mitochondria analogous to the signal recognition particle (*20*). In fungi, mL45 (Mba1) is not a structural component of the mitoribosome (*21*, *22*), whereas in ciliates, a homolog of the bacterial signal recognition particle binding protein Ffh was identified in the mitoribosomal tunnel (*23*). To investigate whether mL45 N terminus recruits OXA1L in human mitochondria, we expressed a variant with a shortened N terminus residues 45 to 74 (ΔN) and showed that although the relative amount of coimmunoprecipitated OXA1L is lower than for the wild type (WT), the truncation of mL45 does not entirely prevent interaction with OXA1L (Fig. 2).

In the inactive state, the basic residues in the mL45 N terminus form electrostatic interactions with the rRNA core that anchor the protein moiety inside the tunnel (Fig. 3A and fig. S11A). In the lower tunnel, mL45 Pro^{68} is stabilized by the mitochondria-specific rRNA

[1]Science for Life Laboratory, Department of Biochemistry and Biophysics, Stockholm University, 17165 Solna, Stockholm, Sweden. [2]Department of Medical Biochemistry and Biophysics, Karolinska Institutet, 17177 Stockholm, Sweden. [3]Department of Neurology, University of Miami Miller School of Medicine, Miami, FL 33136, USA. [4]Institute of Biotechnology, University of Helsinki, 00790 Helsinki, Finland. [5]Faculty of Biological and Environmental Sciences, University of Helsinki, 00790 Helsinki, Finland. [6]Wellcome Centre for Mitochondrial Research, Biosciences Institute, Newcastle University, Newcastle upon Tyne NE2 4HH, UK. [7]Laboratory of Chemical Physics, National Institute of Diabetes and Digestive and Kidney Diseases, National Institutes of Health, Bethesda, MD 20892-0520, USA.
*These authors contributed equally to this work.
†Corresponding author. Email: abarrientos@med.miami.edu (A.B.); brendan.battersby@helsinki.fi (B.J.B.); amunts@scilifelab.se (A.A.)

A1804, mL45 Ile^{76}, and uL23m Leu^{126} (fig. S12A). We found that A1804 is an mtDNA insertion (fig. S8C), which is an unusual feature because only deletions in the mammalian mitochondrial rRNA have been reported to date (*24*–*28*). This stabilization allows mL45 Arg^{61} and Lys^{62} to point toward the rRNA interior (fig. S12A) so that the mL45 N-terminal tail is positioned directly on the nascent-polypeptide path (Fig. 3A). This is further correlated with two hydrophobic residues, Val^{66} and Ile^{67}, forming interprotein hydrophobic pairs with uL23m-α2 (fig. S12A). These interactions stabilize uL23m-α2 perpendicularly to the tunnel so that it fills the spacings at the exit site, blocking the path.

Class 1a* represent the OXA1L-bound state. A continuous density connected to the P-tRNA is observed in the tunnel, corresponding to a nascent polypeptide of a mitoribosome engaged in protein synthesis and associated with OXA1L (fig. S11B). Glu^{70}-Lys^{71} of mL45 adopt a conformation related by ~100°, which results in the 12-Å and 17-Å displacement of the upstream Val^{66} and Ile^{67}, respectively. Therefore, the uL23m-α2 is released and destabilized (Fig. 3B and fig. S12). The loop from the mL45 Tim44-like domain also becomes disordered by losing its interaction with uL23m-α2. The lack of an internal protein scaffold allows the lower tunnel to accommodate a nascent chain. In the upper tunnel, the mL45 membrane-distal tail adopts a folded α helix (α0), stabilized by the mitochondria-specific insertion of uL29m, the β4-β5 hairpin of uL24m, and H50 of rRNA from the opposite sides (Figs. 3B and 4A and fig. S13). Thus, a continuous pathway is formed from the tunnel entrance to the mitoribosomal surface at the membrane-facing region that is available for nascent chain conduction (Fig. 4B and movie S1).

Once folded within the lower tunnel, mL45 forms two mitochondria-specific constriction sites with uL24m (Fig. 4C). The constrictions keep the tunnel width less than 8 Å (Fig. 4D). By contrast, in bacteria, the tunnel increases in diameter to greater than 15 Å, allowing nascent chains to fold in the exit tunnel (*29*). To assess whether mL45-induced geometry of the exit tunnel determines cotranslational protein folding, we used coarse-grained molecular dynamics simulations with WT and Δ*N-mL45* mitoribosomes. Our results show that the observed enclosure of the nascent chain by mL45 decreases helix formation at the constriction sites within the tunnel (fig. S14).

Our data further assign two additional functions to mL45: (i) directing the nascent polypeptide toward the tunnel exit by compensating for rRNA deletion and (ii) positioning the exit at a distance from the membrane surface. The former is achieved by the folded N terminus of mL45, which supports a specific extended-away conformation of the uL24m β4-β5 hairpin rather than extruding into the vestibule, as in bacteria (fig. S8D). As a result, the residues at the hairpin tip that were shown to be implicated in bacterial protein folding (*30*) are 17 Å away, outlining the tunnel walls. This architecture shields an unfolded nascent chain and prevents it from escaping the tunnel prematurely because of rRNA H24 deletion (fig. S8B and D). Then, the positioning of the exit relative to the membrane is mediated by the mL45 Tim44-like domain that allows a gap between the mitoribosomal surface and the insertase, as opposed to a closer association as seen in bacteria (fig. S15). This structural arrangement makes the newly synthesized mitochondrial proteins more accessible for peptidyl deformylase, methionine amino peptidase, and chaperones before the membrane insertion. In yeast, the deletion of mL45 (Mba1) is associated with membrane insertion defects (*31*).

The sequencing of the human mitochondrial genome 40 years ago (*32*) was a turning point in mitochondrial research, postulating a putative specialized mechanism for the synthesis of these 13 transmembrane proteins. Our discovery of mL45-induced conformational changes represents a gating mechanism of the mitoribosome without similarity in bacterial and cytosolic systems. It forms a cavity, secluding unfolded nascent chains and securing their delivery to the membrane. The gating is correlated with the association of the OXA1L insertase; however, secondary structure formation is not favored while a nascent chain is at the constriction sites. Together, the data offer a molecular insight into how proteins are synthesized in human mitochondria.

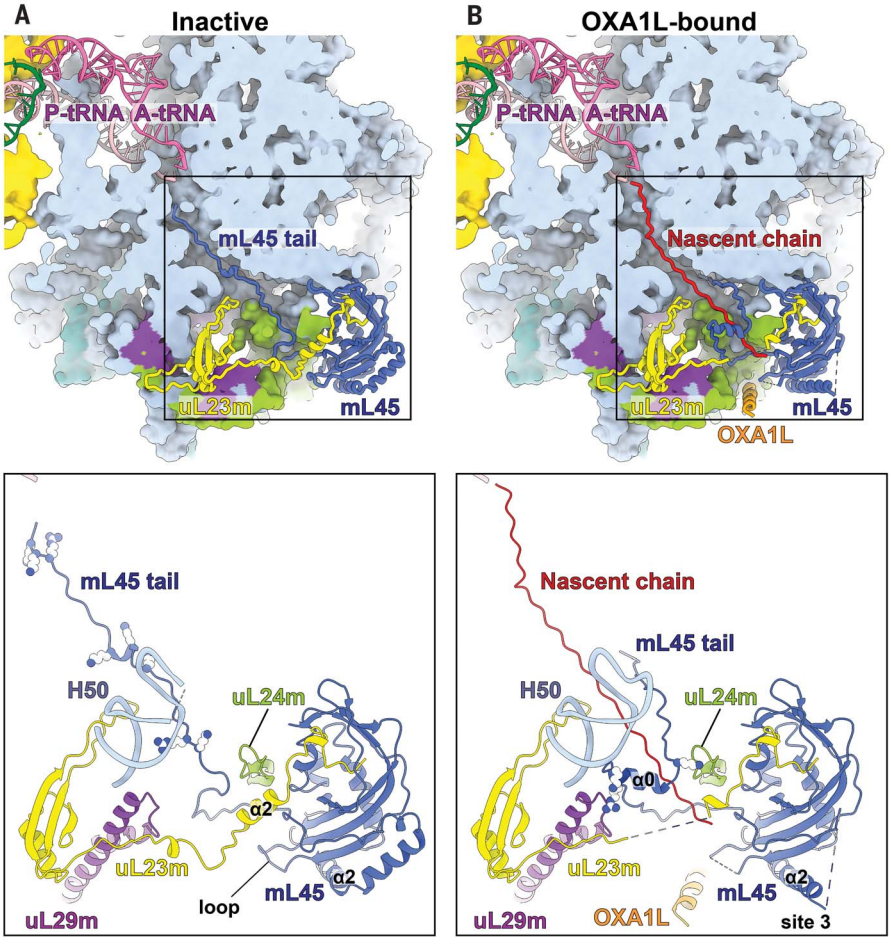

Fig. 3. Comparison between inactive and OXA1L-bound structures. (**A**) In the inactive state, the mL45 N-terminal tail occupies the tunnel. Basic residues in the tunnel are shown as spheres in the bottom panel. uL23m-α2 is stabilized by the mL45 tail and a loop (residues 200 to 208) of mL45. The tip of rRNA Helix 50 (H50) is disordered because of flexibility. (**B**) In the OXA1L-bound state, a nascent polypeptide occupies the tunnel. The mL45 tail is folded and stabilized by uL24m, uL29m, and rRNA H50. The basic residues participating in the stabilization are shown in the bottom panel. The tip of H50 is ordered, uL23m-α2 and the mL45 loop are disordered, and the path through the tunnel is open. The contact site 3 with OXA1L is formed through mL45-α2. The bottom panels show partial structures of uL23m (residues 37 to 153), uL24m (93 to 112), and uL29m (94 to 157).

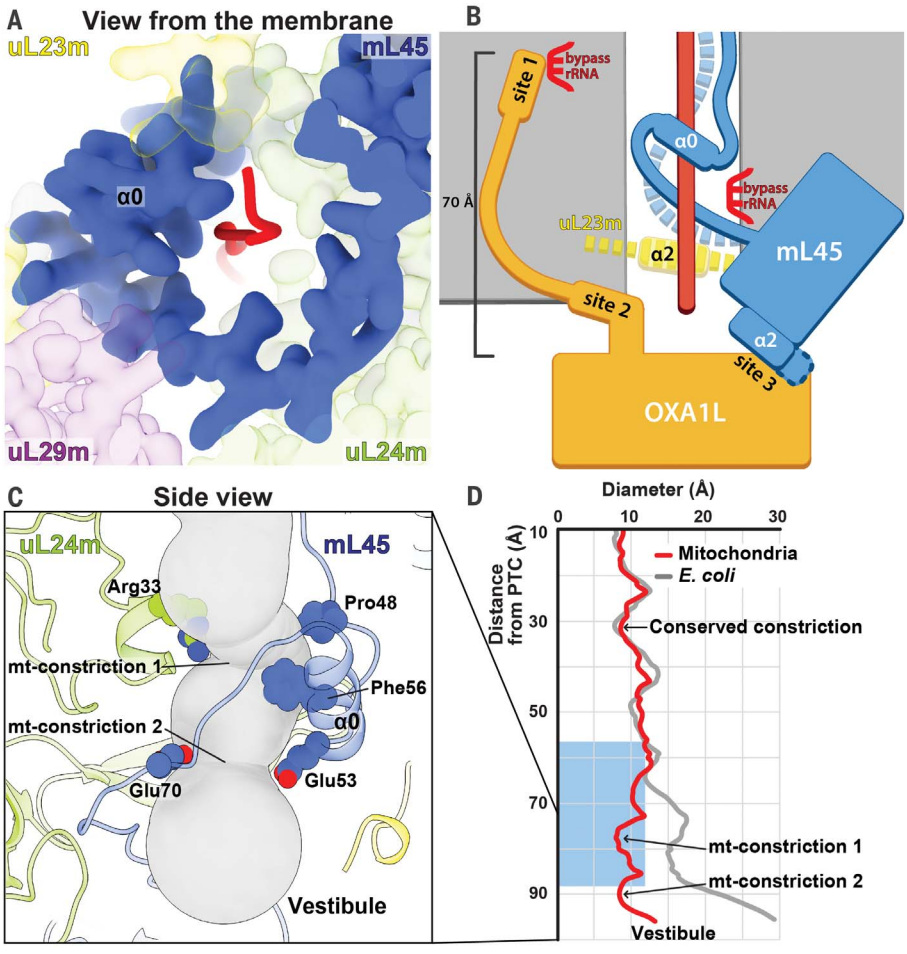

Fig. 4. Mechanism of membrane-tethered nascent-polypeptide emergence. (**A**) Folding of the mL45 tail stabilized by uL29m and uL24m, resulting in a continuous protein arch coating the interior with the nascent chain. (**B**) Side-view schematic of the gating mechanism. The folding of mL45-α0 (blue tube) leads to the detachment of its N terminus from rRNA (dashed blue) and destabilization of uL23m-α2 (dashed yellow) that together open the way for a polypeptide chain (red). OXA1L is docked to the extended mL45-α2 (site 3) for cotranslational insertion of the emerging polypeptide. Contact sites 1 and 2 are formed between the OXA1L-CTE and the mitoribosomal surface up to 70 Å away from the membrane surface. (**C**) Side view of the lower tunnel, shown as a gray tube. Mitochondria-specific constriction sites are formed by mL45-α0 and uL24m, and the involved residues are shown. (**D**) Tunnel diameter was calculated for the mitoribosome and *Escherichia coli* ribosome and plotted along the path. The blue rectangle indicates the position of an α-helical formation within the tunnel in bacteria.

REFERENCES AND NOTES

1. D. De Silva, Y.-T. Tu, A. Amunts, F. Fontanesi, A. Barrientos, *Cell Cycle* **14**, 2226–2250 (2015).
2. A. Suomalainen, B. J. Battersby, *Nat. Rev. Mol. Cell Biol.* **19**, 77–92 (2018).
3. S. Aibara, V. Singh, A. Modelska, A. Amunts, *eLife* **9**, e58362 (2020).
4. R. Englmeier, S. Pfeffer, F. Förster, *Structure* **25**, 1574–1581.e2 (2017).
5. Y. Chen *et al.*, *Structure* **25**, 1403–1414.e3 (2017).
6. E. van Bloois, G. Jan Haan, J.-W. de Gier, B. Oudega, J. Luirink, *FEBS Lett.* **576**, 97–100 (2004).
7. M. van der Laan, P. Bechtluft, S. Kol, N. Nouwen, A. J. M. Driessen, *J. Cell Biol.* **165**, 213–222 (2004).
8. M. Hildenbeutel *et al.*, *J. Mol. Biol.* **423**, 590–599 (2012).
9. L. Jia *et al.*, *EMBO J.* **22**, 6438–6447 (2003).
10. G. Szyrach, M. Ott, N. Bonnefoy, W. Neupert, J. M. Herrmann, *EMBO J.* **22**, 6448–6457 (2003).
11. L. Stiburek *et al.*, *J. Mol. Biol.* **374**, 506–516 (2007).
12. K. Thompson *et al.*, *EMBO Mol. Med.* **10**, e9060 (2018).
13. M. Bañó-Polo *et al.*, *Nat. Commun.* **9**, 5246 (2018).
14. U. Richter *et al.*, *Curr. Biol.* **23**, 535–541 (2013).
15. J. Zivanov *et al.*, *eLife* **7**, e42166 (2018).
16. S. Wickles *et al.*, *eLife* **3**, e03035 (2014).
17. A. Kedrov *et al.*, *Cell Rep.* **17**, 2943–2954 (2016).
18. R. G. Lee *et al.*, *J. Cell Sci.* **133**, jcs240374 (2020).
19. Y.-T. Tu, A. Barrientos, *Cell Rep.* **10**, 854–864 (2015).
20. E. Kummer *et al.*, *Nature* **560**, 263–267 (2018).
21. A. Amunts *et al.*, *Science* **343**, 1485–1489 (2014).
22. Y. Itoh, A. Naschberger, N. Mortezaei, J. M. Herrmann, A. Amunts, *Nat. Commun.* **11**, 5187 (2020).
23. V. Tobiasson, A. Amunts, *eLife* **9**, e59264 (2020).
24. B. J. Greber *et al.*, *Nature* **515**, 283–286 (2014).
25. A. Amunts, A. Brown, J. Toots, S. H. W. Scheres, V. Ramakrishnan, *Science* **348**, 95–98 (2015).
26. B. J. Greber *et al.*, *Science* **348**, 303–308 (2015).
27. A. Brown *et al.*, *Nat. Struct. Mol. Biol.* **24**, 866–869 (2017).
28. A. S. Petrov *et al.*, *Mol. Biol. Evol.* **36**, 207–219 (2019).
29. M. Liutkute, E. Samatova, M. V. Rodnina, *Biomolecules* **10**, 97 (2020).
30. R. Kudva *et al.*, *eLife* **7**, e36326 (2018).
31. H. Bauerschmitt *et al.*, *Mol. Biol. Cell* **21**, 1937–1944 (2010).
32. S. Anderson *et al.*, *Nature* **290**, 457–465 (1981).

ACKNOWLEDGMENTS

We thank SciLifeLab for access to the cryo-EM facility (funded by the KAW, EPS, and Kempe foundations) and clinical proteomics mass spectrometry facility; Diamond Light Source for access to eBIC (funded by the Wellcome Trust, MRC, and BBSRC) under proposal EM19823-1 with assistance from Y. Chaban; and R. Kock Flygaard and N. Fluman for advice. **Funding:** Swedish Foundation for Strategic Research (FFL15:0325), Ragnar Söderberg Foundation (M44/16), Cancerfonden (2017/1041), European Research Council (ERC-2018-StG-805230), Knut and Alice Wallenberg Foundation (2018.0080), The Academy of Finland (307431 and 314706 to B.J.B.), Sigrid Juselius Foundation (to B.J.B), NIH-R35 grant (GM118141 to A.B.), and MDA Research Grant (MDA-381828 to A.B.) supported this work. R.B.B. was supported by the Intramural Research Program of the National Institute of Diabetes and Digestive and Kidney Diseases of the NIH. This work used the computational resources of the NIH HPC Biowulf cluster (https://hpc.nih.gov). Y.I. was supported by H2020-MSCA-IF-2017 (799399-Itohribo). P.M. is the recipient of a postdoctoral fellowship from the American Heart Association (19POST34450174). **Author contributions:** B.J.B., U.R., and A.A. designed the project. J.A., U.R., and A.A. prepared the sample for cryo-EM. J.A. and Y.I. collected and processed the cryo-EM data. Y.I. built the model. A.C., P.M., and A.B. performed biochemical analysis. R.B.B. performed molecular simulation. A.A., Y.I., and J.A. wrote the manuscript with contributions from all coauthors. **Competing interests:** The authors declare no competing interests. **Data and materials availability:** The atomic coordinates were deposited in the RCSB Protein Data Bank (PDB) under accession numbers 6ZM5 and 6ZM6. The cryo-EM maps have been deposited in the Electron Microscopy Data Bank (EMDB) under accession numbers EMD-11278, EMD-11279, EMD-11280, EMD-11281, EMD-11282, EMD-11283, EMD-11284, EMD-11285, EMD-11286, and EMD-11287.

SUPPLEMENTARY MATERIALS

science.sciencemag.org/content/371/6531/846/suppl/DC1
Materials and Methods
Figs. S1 to S15
Tables S1 to S5
References (*33*–*61*)
MDAR Reproducibility Checklist
Movie S1

View/request a protocol for this paper from *Bio-protocol*.

29 July 2020; accepted 24 December 2020
10.1126/science.abe0763

Mechanism of membrane-tethered mitochondrial protein synthesis

Yuzuru Itoh, Juni Andréll, Austin Choi, Uwe Richter, Priyanka Maiti, Robert B. Best, Antoni Barrientos, Brendan J. Battersby and Alexey Amunts

Science **371** (6531), 846-849.
DOI: 10.1126/science.abe0763

Making the energy makers

Within a mitochondrion, the powerhouse of eukaryotic cells, synthesis of the specialized transmembrane proteins of the electron transport chain is performed by dedicated mitoribosomes. The mechanism by which mitoribosomes couple protein synthesis with membrane insertion is poorly understood. Itoh *et al.* determined structures of the human mitoribosome during nascent chain synthesis while bound to its membrane insertase. These structures revealed a series of coordinated conformational changes within the polypeptide exit tunnel. The gating mechanism offers a fundamental molecular insight into how membrane proteins are synthesized in human mitochondria.

Science, this issue p. 846